

OPEN ACCESS

$\text{Si}_{85}\text{Fe}_{15}\text{O}_x$ Alloy Anode Materials with High Thermal Stability for Lithium Ion Batteries

To cite this article: Yijia Liu *et al* 2021 *J. Electrochem. Soc.* **168** 110521

View the [article online](#) for updates and enhancements.



ECS Membership = Connection

ECS membership connects you to the electrochemical community:

- Facilitate your research and discovery through ECS meetings which convene scientists from around the world;
- Access professional support through your lifetime career;
- Open up mentorship opportunities across the stages of your career;
- Build relationships that nurture partnership, teamwork—and success!


Join ECS!

Visit electrochem.org/join





Si₈₅Fe₁₅O_x Alloy Anode Materials with High Thermal Stability for Lithium Ion Batteries

Yijia Liu,¹ Michael Charlton,¹ Jun Wang,¹ J. Craig Bennett,² and M. N. Obrovac^{1,3,*} 

¹Department of Chemistry, Dalhousie University, Halifax, N.S., B3H 4R2 Canada

²Department of Physics, Acadia University, Wolfville, N.S., B4P 2R6, Canada

³Department of Physics and Atmospheric Science, Dalhousie University, Halifax, N.S., B3H 4R2, Canada

The synthesis, microstructure and electrochemical properties of ball milled Si₈₅Fe₁₅O_x alloys with different oxygen contents are investigated. These materials combine the features of Si-M alloys (low irreversible capacity) and SiO_x materials (high thermal stability). This makes Si₈₅Fe₁₅O_x alloys compatible with high temperature processing. As shown here, these properties allow Si₈₅Fe₁₅O_x alloys to be incorporated into carbon-coated graphite composite particles that can cycle well even without the use of advanced binders or electrolyte additives.

© 2021 The Author(s). Published on behalf of The Electrochemical Society by IOP Publishing Limited. This is an open access article distributed under the terms of the Creative Commons Attribution Non-Commercial No Derivatives 4.0 License (CC BY-NC-ND, <http://creativecommons.org/licenses/by-nc-nd/4.0/>), which permits non-commercial reuse, distribution, and reproduction in any medium, provided the original work is not changed in any way and is properly cited. For permission for commercial reuse, please email: permissions@iopublishing.org. [DOI: [10.1149/1945-7111/ac3163](https://doi.org/10.1149/1945-7111/ac3163)]



Manuscript submitted April 21, 2021; revised manuscript received September 27, 2021. Published November 11, 2021.

Supplementary material for this article is available [online](#)

Si-based alloy negative electrode materials have received lots of attention because of their large volumetric capacity compared to graphite. Theoretically, the use of Si-based anodes can result in up to 20% increase in Li-ion cell volumetric energy density. However, Si-based anodes can have poor cycling characteristics as a result of their large volume change upon lithiation (280% increase in volume for the full lithiation of pure Si). Repeated lithiation and delithiation during cell cycling can result in particle fracture and disruption of the solid electrolyte interphase, causing cell fade. Cell fade can be reduced if nanostructured or amorphous Si-based alloys are used, which have reduced volume expansion and in which the a-Li_xSi—Li₁₅Si₄ phase transition is suppressed. For example, excellent cycling in Si-M (M = transition metal) has been demonstrated.^{1–10} Iron is an excellent candidate as a component for Si-based alloy anodes due to its high earth abundance, low cost, and formation of inactive silicides with good conductivity. For these reasons, the Fe-Si system has been intensively studied and prepared by various methods (such as magnetron sputtering, ball milling, reduction, and spark plasma) in recent years.^{4,8,9,11–24} However, Si-based alloys still suffer from side reactions with electrolyte during cycling, although the rate of these reactions is greatly reduced.²⁵ SiO_x has also been extensively studied as an anode material because of reduced volume expansion, less side reactions with electrolyte, and high capacity retention during cycling.²⁶ However, the first cycle coulombic efficiency of SiO_x is low because of the irreversible formation of lithium silicates.²⁷ In addition, the preparation method of SiO_x can be expensive.²⁸ Recently we reported that SiO_x can be made by ball milling Si in air, which may represent a low cost processing route.²⁸ SiO_x has an additional advantage in that it can maintain its amorphous microstructure, even when heated to high temperatures, e.g., 800 °C. Indeed, such thermal treatment has been reported to improve its capacity retention. Such high temperature stability also makes it compatible with carbon coating by chemical vapor deposition (CVD), which has been shown to improve its capacity retention further.

Recently we reported that Si-alloy particles made by ball milling can be embedded within graphite particles by mechanofusion processing.²⁹ Ball milled particles are ideal for this purpose, since they typically have primary particle sizes of ~0.5 μm, which can be embedded into ~10 μm graphite particles without changing their morphology. We have found that particles larger than 1 μm in size

will not become embedded by this process. Therefore, it is important for the embedded alloy to be ~0.5 μm in size. However, even when the alloy is fully embedded within graphite particles, electrolyte can still permeate into such particles via their porosity and react with the embedded alloys within, causing cell fade. We have shown that applying a carbon coating to the composite particles by CVD can eliminate electrolyte infiltration. The goal of this study is to create alloy particles that can be embedded within graphite particles by mechanofusion to create composite particles that can be subsequently carbon-coated to eliminate electrolyte/alloy interactions, while maintaining good cycling properties and low irreversible capacity. In order to achieve this, the Si-alloy should have the following properties:

- ~0.5 μm primary particle size
- low irreversible capacity
- retains nanostructured Si phase when heated to CVD processing temperatures (~800 °C)

Here we show that ball milled Si₈₅Fe₁₅O_x alloys, which combine the low irreversible capacity of Si-M alloys with the high thermal stability of SiO_x are promising candidate alloy particles with the above properties. The Si₈₅Fe₁₅O_x were embedded into spherical natural graphite and CVD-coated to create high performance composite anode particles.

Experimental

Silicon (325 mesh, 99%, Aldrich) and iron (325 mesh, 99.9%, Aldrich) powders in a stoichiometric ratio of 85:15 were ball milled in a SPEX 8000-D mill (SPEX Certiprep, Metuchen, N.J.) using the optimized conditions described in Ref. 30, 180 g of 1.6 mm 440C stainless steel balls, 65 ml hardened steel container, 0.5 ml total volume of sample powders, based on the powder bulk density. Total milling time was fixed at 16 h, but with different milling periods in argon atmosphere or in air as indicated in Fig. S1 (available online at stacks.iop.org/JES/168/110521/mmedia), in order to control the oxygen content. Milling in an Ar atmosphere was accomplished by sealing the milling vessel in an Ar-filled glovebox prior to milling. Milling in air was accomplished by “sealing” the milling vessel in air with the o-ring seal removed prior to milling. This maintained the sample powder within the vessel, but allowed air to flow in or out during milling. Ethanol (99.89%, containing 0.10% H₂O, Commercial Alcohols) was used for sample recovery. Sample vials were half filled with ethanol and milled for five more minutes. The resulting ethanol slurry was then collected in a pan and dried in

*Electrochemical Society Member.

^zE-mail: mnobrovac@dal.ca

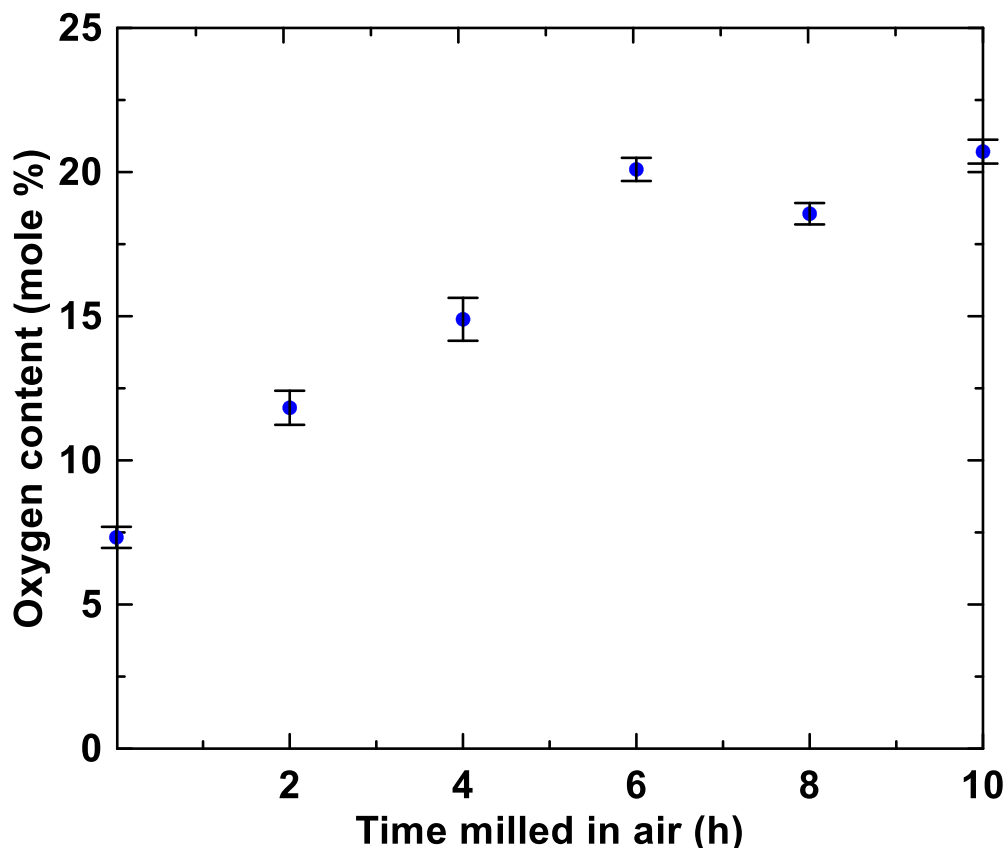


Figure 1. Oxygen content of $\text{Si}_{85}\text{Fe}_{15}\text{O}_x$ alloys versus air milling time. The accuracy of the LECO method is $\pm 2\%$ for elements in the range of 10%–25% and $\pm 5\%$ for elements in the range of 3%–10% of the reported values (provided by NSL).

a solvent oven at 120 °C in air. Some samples were subsequently heated in a tube furnace at 600 °C and 800 °C for 3 h under an argon flow. The resulting $\text{Si}_{85}\text{Fe}_{15}\text{O}_x$ alloys are identified here according to their air milling time, e.g., $\text{Si}_{85}\text{Fe}_{15}\text{O}_x(4 \text{ h/air})$. Composite alloy/graphite particles were made by embedding 14.2 wt.% $\text{Si}_{85}\text{Fe}_{15}\text{O}_x(10 \text{ h/air})$ alloy into spherical natural graphite particles (Asbury A3901). 33 g of a 1:6 by mass mixture of $\text{SiFe}_{0.20}\text{O}_{0.39}$ alloy and graphite was dry processed using a 10 cm diameter mechanofusion machine (Dry Particle Fusion Machine, DPM Solutions, Hebbleville NS Canada). Mechanofusion was conducted at 2500 rpm with a 1 mm press-head/wall gap to embed the alloy into the graphite particles. CVD carbon coating was applied to the MF-processed $\text{SiFe}_{0.20}\text{O}_{0.39}$ /graphite composite using flowing ethylene gas as the carbon source at 800 °C in a rotating fluidized bed for 1 or 2 h, followed by 1 h of argon flow. Oxygen contents of alloy samples were determined by LECO analysis by NSL Analytical of Cleveland, OH. X-ray diffraction patterns of $\text{Si}_{85}\text{Fe}_{15}\text{O}_x$ alloys were collected with a Rigaku Ultima IV diffractometer equipped with a Cu target, a dual-position graphite diffracted beam monochromator, and a scintillation counter detector. True sample densities were measured using a Micromeritics AccuPyc II 1340 Pycnometer. SEM images and elemental analysis were obtained using an EDS attached TESCAN MIRA 3 field-emission electron microscope. Transmission electron microscope (TEM) images were taken using a Philips CM30 TEM. TEM specimens were made by suspending as-received powder in methanol, sonicating for 5 min, and placing a drop onto a lacey carbon coated TEM grid.

Electrochemical tests were conducted by first incorporating alloy powders in electrodes as follows. Powders of Si-Fe-O alloys were mixed with carbon black (Super C65, Imerys Graphite and Carbon) and a 10 wt.% aqueous solution of lithium polyacrylate (LiPAA) at a volumetric ratio of 70/5/25 in distilled water using a planetary ball

mill (Retsch PM 200) with two 11 mm WC balls at 100 rpm for 1 h. A thin layer of slurry was coated on Cu foil (Furukawa Electric, Japan) using a 0.1 mm coating bar. The coating was then dried in air at 120 °C for 1 h. The alloy electrodes were incorporated into 2325 type coin cells with Li metal as the counter/reference electrode and 1 M LiPF_6 (BASF) in a solution of FEC: EC: DEC (1:3:6 by volume, BASF) electrolyte. The electrodes were separated by two layers of Celgard 2300 separators. Typical loadings were 2.07 mg cm^{-2} , corresponding to 2.45 mAh cm^{-2} for a sample with 1180 mAh/g specific capacity. Electrochemical tests were performed using a Neware Test System. Coin cells were cycled at 30 °C, between 5 mV and 0.9 V at a rate of C/20 and signature discharged (lower currents in steps with a relaxation time between each current change) to C/40 for the first cycle; and at a C/10 and signature discharged to C/20 for subsequent cycles.

Results and Discussion

Figure 1 shows the oxygen content of the $\text{Si}_{85}\text{Fe}_{15}\text{O}_x$ alloys as a function of time milled in air. At zero milling time, the oxygen content is about 7 at.%. This is consistent with the amount of oxygen present in the raw material powders before milling.³¹ From 0 h to 6 h air milling time, the oxygen contents linearly increase with the time milled in air until an oxygen composition of about 20 at.% is reached. After 6 h, there is no significant change in the oxygen content even when the air milling time was increased to 10 h. The same trend has been observed for reactive ball milling of Si in air to make SiO_x in which the maximum oxygen content that could be achieved by reactive ball milling was $\text{SiO}_{0.37}$. As the alloy particles become fractured, new surfaces react with the air, until the particles become too small to fracture, at which point no further reaction occurs.³² Therefore, the samples range in composition from

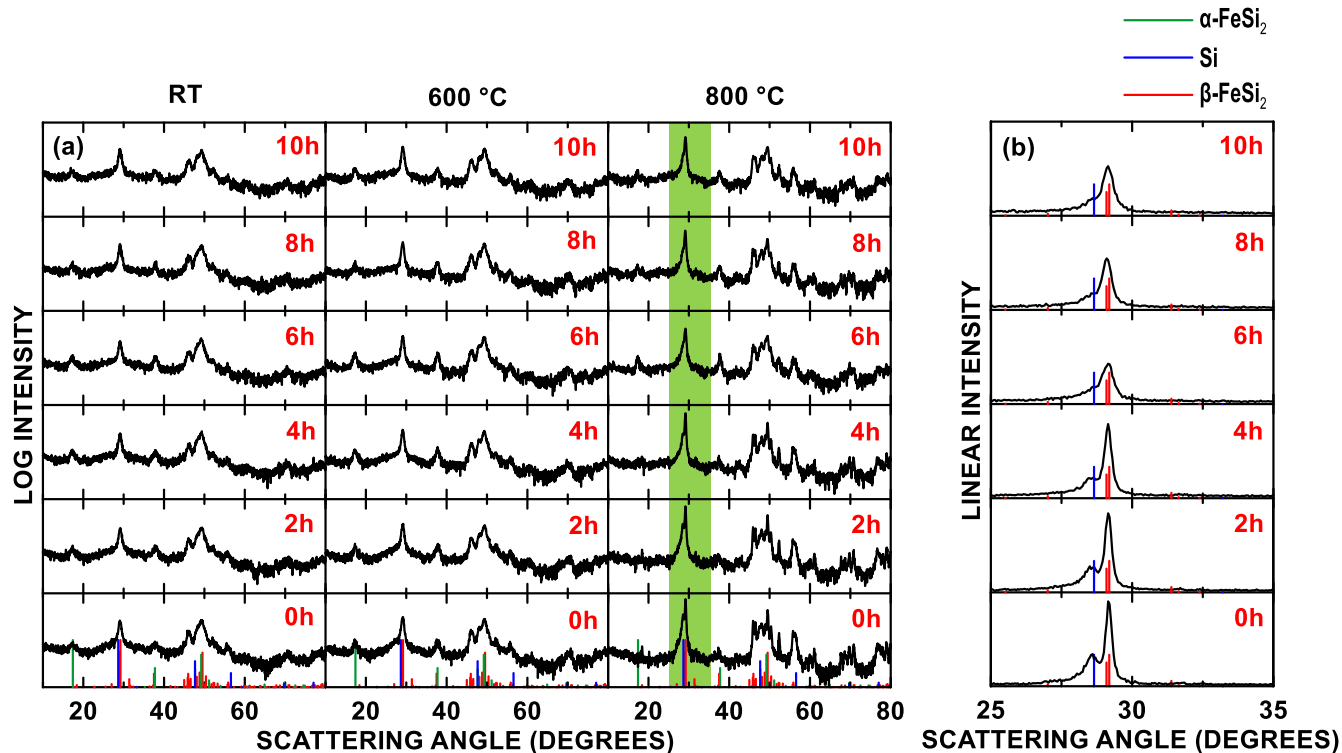


Figure 2. (a) XRD patterns of $\text{Si}_{85}\text{Fe}_{15}\text{O}_x$ alloys as milled and after thermal annealing at 600 °C and 800 °C. Known phase peak positions and intensities are indicated by vertical lines. (b) Expanded XRD patterns of highlighted regions in (a).

$[\text{Si}_{0.85}\text{Fe}_{0.15}]_{93}\text{O}_7$ (0 h air milled sample) to $[\text{Si}_{0.85}\text{Fe}_{0.15}]_{80}\text{O}_{20}$ (6–10 h air milled samples). This corresponds to a maximum O:Si ratio of 0.29. However, if it is assumed that the iron has reacted with the Si to make FeSi_2 , as suggested by XRD results below, then the O:(unreacted Si) ratio is 0.45, which is somewhat higher than the maximum O:Si ratio of 0.37 achieved for reactive ball milled SiO_x .³² The iron content was 14.8 ± 0.6 at.% (metals basis) for all samples according to EDS elemental analysis and had no dependence on the air milling time. This indicates that the Fe contamination from milling was insignificant compared to the overall Fe content.

Figure 2 shows powder XRD patterns of ball milled $\text{Si}_{85}\text{Fe}_{15}\text{O}_x$ alloys at different air milling times. Peaks of known phases are indicated. The as-milled $\text{Si}_{85}\text{Fe}_{15}\text{O}_x$ alloys are composed of $\alpha\text{-FeSi}_2$ (PDF: 00–089–2024), $\beta\text{-FeSi}_2$ (PDF: 00–071–0642) and an amorphous phase consistent with broad intensities consistent with Si or SiO_x . Here $\alpha\text{-FeSi}_2$ is the high temperature (>937 °C) stable phase of FeSi_2 and $\beta\text{-FeSi}_2$ is the low-temperature stable phase (<937 °C). The preferential formation of metastable $\alpha\text{-FeSi}_2$ during ball milling Fe and Si has been reported previously.^{13,33} Samples prepared with different air milling times have very similar XRD patterns, despite having significant differences in oxygen content, as discussed above. Figure S2 shows SEM images of as-milled $\text{Si}_{85}\text{Fe}_{15}\text{O}_x$ alloys. It was found that $\text{Si}_{85}\text{Fe}_{15}\text{O}_x$ alloys made with different air milling times have very similar morphologies. The samples are all composed of submicron to micron-sized particles as significant size reduction occurred during the mechanical milling process. In all samples some primary and secondary particles that are up to 5 μm in size are present in the SEM images. Increasing air milling time does not significantly change the morphology of the $\text{Si}_{85}\text{Fe}_{15}\text{O}_x$ alloy particles. Figure S3 shows the particle size distribution of the 10 h air milled $\text{Si}_{85}\text{Fe}_{15}\text{O}_x$ alloys. A substantial amount of the alloy powder is greater than 1 μm . This particle size range is not ideal for embedding into graphite by mechanofusion. As will be shown below, primary and secondary particles greater than about 1 μm do not become embedded into graphite. Further particle size

reduction is needed to improve the compatibility of this alloy with the embedding process. Nevertheless, as will also be shown below, impressive improvements in cycling can be obtained even when a portion of the alloy is embedded into graphite. TEM images of 0 h and 8 h air milled $\text{Si}_{85}\text{Fe}_{15}\text{O}_x$ alloys are shown in Figs. 3a and 3b. The images show dark regions that are about 10–20 nm in size surrounded by a lighter matrix. Dark areas correspond to those that are electron-rich, while light regions correspond to those that are electron poor. In this case, this suggests that the dark regions are those that include Fe and the light regions do not include Fe. Combining with XRD results suggests that the dark regions are FeSi_2 phases, while the light regions consist of Si or SiO_x . Figure S4a shows an electron diffraction pattern of $\text{Si}_{85}\text{Fe}_{15}\text{O}_x$ (0 h). The most intense rings in the diffraction pattern are consistent with $\beta\text{-FeSi}_2$ or Si, which is consistent with XRD results. Diffuse rings are also present, suggesting the presence of amorphous phases. This suggests that any oxygen containing phase present is amorphous. These observations are consistent with the alloys comprising 10–20 nm FeSi_2 grains surrounded by an amorphous Si-O matrix. In summary, significant differences in the $\text{Si}_{85}\text{Fe}_{15}\text{O}_x$ alloys could not be detected by SEM, XRD, or TEM measurements, despite significant differences in the oxygen contents in these samples.

Differences between the alloys became apparent after the samples were heated. The diffraction patterns of ball milled $\text{Si}_{85}\text{Fe}_{15}\text{O}_x$ alloys before and after annealing at 600 °C and 800 °C are shown in Fig. 2. The XRD patterns of 600 °C annealed $\text{Si}_{85}\text{Fe}_{15}\text{O}_x$ alloys are almost identical to the unheated $\text{Si}_{85}\text{Fe}_{15}\text{O}_x$ alloys, indicating that no phase transitions or crystal growth detectable by XRD occurs at 600 °C. At 800 °C, the $\beta\text{-FeSi}_2$ phase, which is the thermodynamically stable phase at 800 °C, crystallizes and becomes the dominant silicide phase in the XRD patterns for all the 800 °C annealed alloys, while the $\alpha\text{-FeSi}_2$ peaks almost disappear. After heating to 800 °C a distinct peak also appears at about 28° for samples ball milled in air for 4 h or less. This peak (highlighted in green) corresponds to the Si (111) peak, indicating

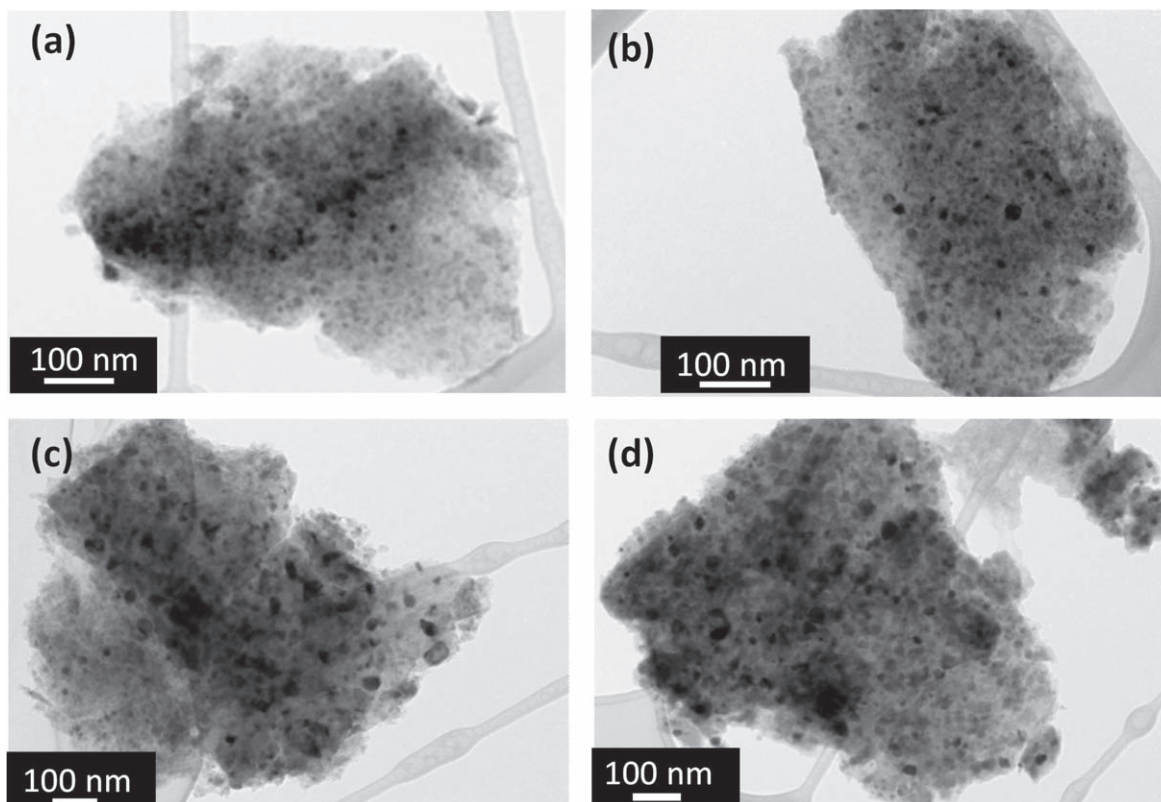


Figure 3. TEM images of (a) $\text{Si}_{85}\text{Fe}_{15}\text{O}_x(0 \text{ h})$, (b) $\text{Si}_{85}\text{Fe}_{15}\text{O}_x(8 \text{ h})$, (c) $600 \text{ }^\circ\text{C}$ annealed $\text{Si}_{85}\text{Fe}_{15}\text{O}_x(8 \text{ h})$, and (d) $800 \text{ }^\circ\text{C}$ annealed $\text{Si}_{85}\text{Fe}_{15}\text{O}_x(8 \text{ h})$ alloys.

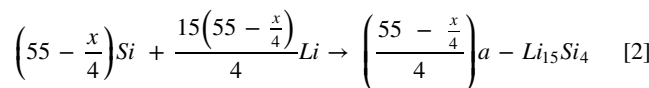
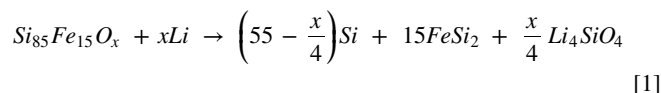
that crystallization of elemental Si occurs in these samples during heating. The intensity of this peak is highly correlated to the air milling time, with the peak becoming smaller as the air milling time is increased. This is understandable, since with longer milling time in air, the amount of elemental Si should reduce, as Si reacts to form SiO. In contrast to the samples with low oxygen content, the samples with greater than 4 h air milling time show no evidence of crystalline Si formation after heating to $800 \text{ }^\circ\text{C}$, indicating excellent thermal stability.

TEM images were also obtained for the heated $\text{Si}_{85}\text{Fe}_{15}\text{O}_x$ alloys, as shown in Figs. 3c–3d for the case of the $\text{Si}_{85}\text{Fe}_{15}\text{O}_x(8 \text{ h/air})$ alloy. In general, the overall microstructure is well-maintained even after heating to $800 \text{ }^\circ\text{C}$. Cao et al. have found that the isolated Si nanocrystallites in ball milled SiO_x materials (prepared in a similar way as the study conducted here) maintain their size ($<10 \text{ nm}$) even after heating to $800 \text{ }^\circ\text{C}$.²⁸ This may be similar to the observed behavior of the Si phase in the $\text{Si}_{85}\text{Fe}_{15}\text{O}_x(8 \text{ h/air})$ alloy. However, the FeSi_2 phases in the $\text{Si}_{85}\text{Fe}_{15}\text{O}_x$ alloys complicates the interpretation of the TEM images, making it hard to differentiate changes in the Si nanocrystallites during the annealing process. From the TEM and XRD results, it appears that the $800 \text{ }^\circ\text{C}$ annealed samples with $>4 \text{ h}$ air milling time comprise small ($\sim 10 \text{ nm}$) Si nanocrystallites and FeSi_2 nanocrystallites with larger crystallite sizes. Further confirmation is provided by the electrochemical studies below.

Figure 4 shows the potential profiles and corresponding differential capacity curves (first three cycles) of the $\text{Si}_{85}\text{Fe}_{15}\text{O}_x(0\text{--}10 \text{ h/air})$ alloys. The observed first cycle reversible capacity decreases as air milling time increases, changing from about 1600 mAh g^{-1} to 1200 mAh g^{-1} , due to the reaction between Si and oxygen, resulting in the loss of active Si. Figure 5 shows the predicted and experimental capacities of the alloys during first lithiation and delithiation. The predicted capacities were calculated according to the following model. According to XRD and TEM results, all Fe has reacted with Si to form inactive FeSi_2 during ball milling and the only active phases present in the as-made alloy are

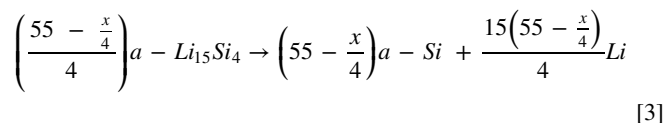
$\text{SiO}_{2-\delta}$ and amorphous Si. The first lithiation process can therefore be described as follows:

First lithiation:



The products of these reactions are Li_4SiO_4 (corresponding to the reaction that occurs at the oxygen plateau, the formation of this phase being irreversible at potentials below 1 V) and amorphous lithiated silicon, which is assumed here to have the same composition as $\text{Li}_{15}\text{Si}_4$ (the highest lithiated phase of silicon achievable at room temperature). During the first delithiation process, the amorphous $a\text{-Li}_{15}\text{Si}_4$ phase becomes delithiated, to form amorphous Si, which is shown in Eq. 3.

First delithiation:



This model has been shown to work well for ball milled FeSi_2 and SiO_x alloys^{13,32} and sputtered Si-Fe-O alloys.⁴ Here, the model also works well for the $\text{Si}_{85}\text{Fe}_{15}\text{O}_x(0 \text{ h/air})$ sample. For this sample, the theoretical lithiation capacity is larger than predicted (as expected from SEI formation), while the delithiation capacity is nearly exactly as predicted. For higher oxygen contents, the measured lithiation and delithiation capacities become reduced

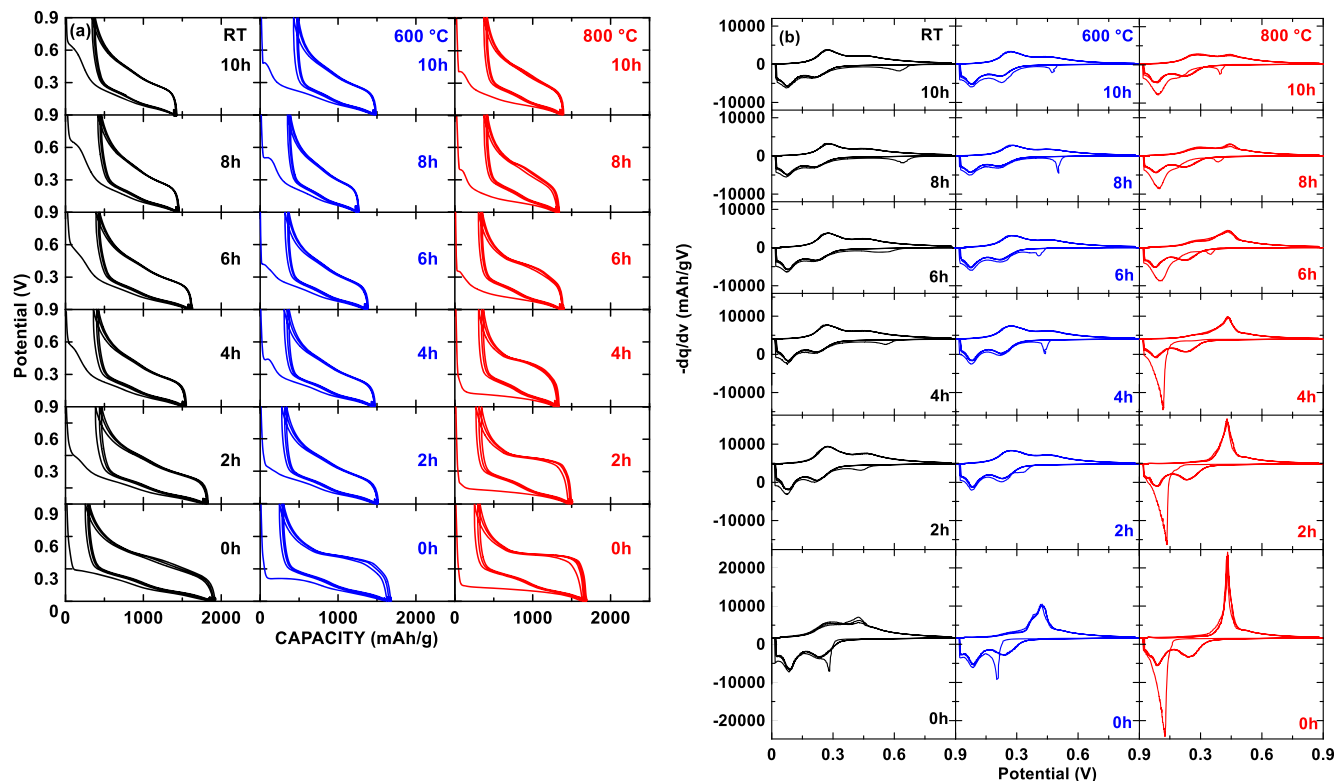


Figure 4. (a) Potential profiles of Si₈₅Fe₁₅O_x alloys (with different air milling time) as milled and after thermal annealing at 600 °C and 800 °C. (b) Differential capacity as a function of potential of the alloys shown in Fig. 4a.

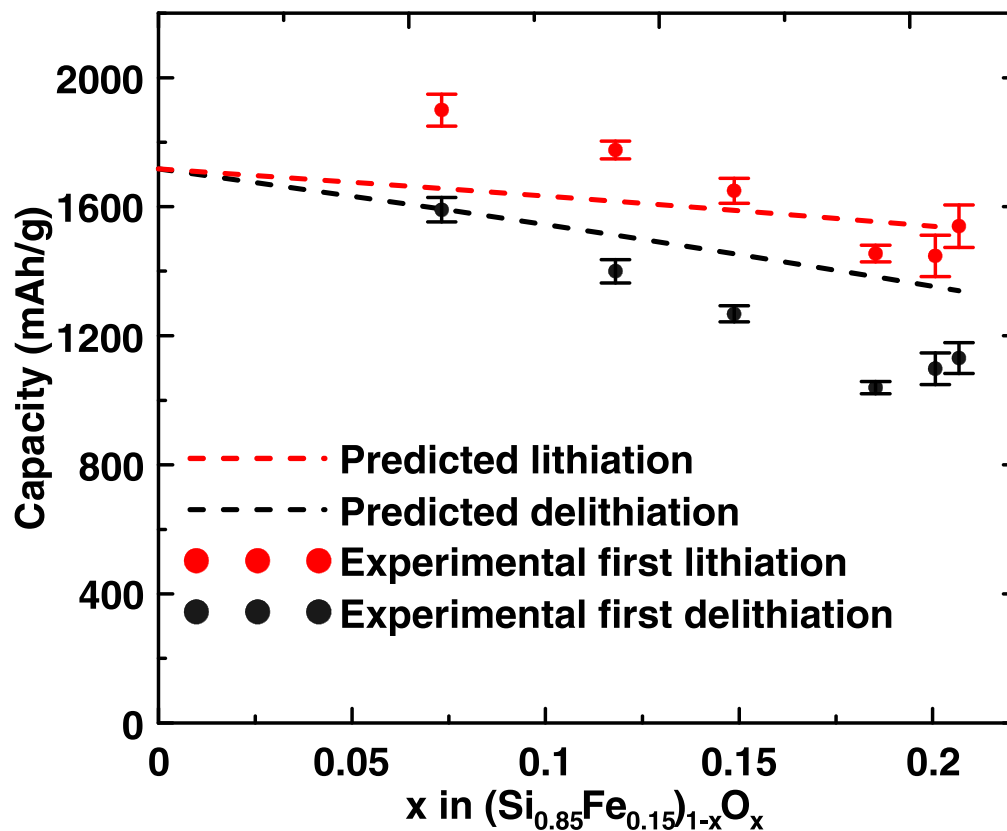


Figure 5. The first lithiation and delithiation capacities of ball milled Si₈₅Fe₁₅O_x alloys as a function of oxygen content.

with increasing oxygen content at a rate that is faster than predicted by the model. It is difficult to understand the reason for this. As will be shown below, capacities become even further reduced after thermal treatment. We speculate that as the inactive phase fraction increases some active Si in these samples may become completely surrounded and isolated by inactive phases, thereby becoming inaccessible towards lithiation. This behavior has also been observed in SiO, where isolated Si species also exist and the fraction of isolated Si increases with thermal treatment, resulting in reduced capacity.³⁴ Further details about the thermal treatment of these samples will be discussed below.

A small plateau at 0.45–0.65 V in the potential profiles (Fig. 4a) and a corresponding peak in the differential capacity curves (Fig. 4b) during the first lithiation is observed for all the air milled alloys and disappears in the following cycles. In SiO_x made by reactive air milling, this first lithiation high potential plateau is believed to be associated with the irreversible formation of Li₄SiO₄ at oxygen defect sites.^{4,32} The potential and capacity of this plateau have been found to increase with increasing oxygen content.^{4,32} This was also found to be the case here. Figure S5 shows an overlay of the first lithiation differential capacity curves of all the alloys, in which it can clearly be seen that both the potential and the area under this peak increase with increasing air milling time/oxygen content. This is quantified in Fig. 6 in which the amount of Li inserted per mole of (Si_{0.85}Fe_{0.15})_{1-x}O_x during the initial 0.45–0.65 V lithiation potential plateau is plotted as a function of the oxygen content. Also plotted in this figure is the Li extracted during delithiation between 0.9 V and 2 V for each alloy (differential capacity curves of the alloys cycled above 0.9 V are shown in Fig. S6). The amount of Li extracted above 0.9 V has been shown to be directly correlated to the amount of oxygen in ball milled and sputtered SiO_x.^{27,32} As the oxygen content increases, the amount of Li associated with the high potential initial lithiation plateau and the capacity above 0.9 V both increase linearly. In addition, the slope of both plots is close to 1, which is consistent

with the formation of Li₄SiO₄ (Li:O = 1:1) during the first lithiation. This is also consistent with earlier studies of SiO_x.^{27,32} This result shows that all the oxygen in the sample can be converted to the Li₄SiO₄ phase, as in the case of ball milled and sputtered SiO_x, confirming Eq. 1 in the above capacity model. It furthermore verifies the accuracy of the measured oxygen contents in these samples.

During the initial lithiation, subsequent to the high potential plateau, a sharp peak at about 0.28 V in some of the Si₈₅Fe₁₅O_x alloys was also observed. This peak has been associated with a nucleation and growth process for the initial lithiation step of Si.³⁵ As lithiation progresses, two broad peaks are then observed, corresponding to two single-phase lithiation processes that occur for amorphous Si. During delithiation, two corresponding broad peaks are observed which correspond to the delithiation of amorphous Si.³⁶ No pronounced peak at around 0.43 V, associated with Li₁₅Si₄ delithiation, were observed for any sample, indicating that Li₁₅Si₄ formation is fully suppressed during the lithiation of these alloys. The suppression of Li₁₅Si₄ formation is thought to be due to stress-potential coupling between the active Si and the inactive phases in Si-M alloys^{18,37,38} and is thought to enhance cycling performance, since the two-phase Li₁₅Si₄ delithiation reaction is avoided.

Figure 7a shows the specific capacity vs cycle number of ball-milled Si₈₅Fe₁₅O_x alloys. Si₈₅Fe₁₅O_x(0 h/air) suffers from capacity fade. With increasing air milling time, the initial reversible capacity decreases as the amount of active Si is reduced, as discussed above. However, improved cycling performance was obtained with increasing air milling time, likely as the result of increased inactive phase and reduced volume expansion. The inactive Li-O species formed during the first lithiation not only can reduce the overall volume expansion of Si₈₅Fe₁₅O_x alloys, but also improve the ion conductivity.^{39–42} The 10 h air milled alloys have the highest capacity retention of about 1100 mAh/g after 50 cycles. Figure S7 shows the initial coulombic efficiency (ICE) vs. oxygen content in

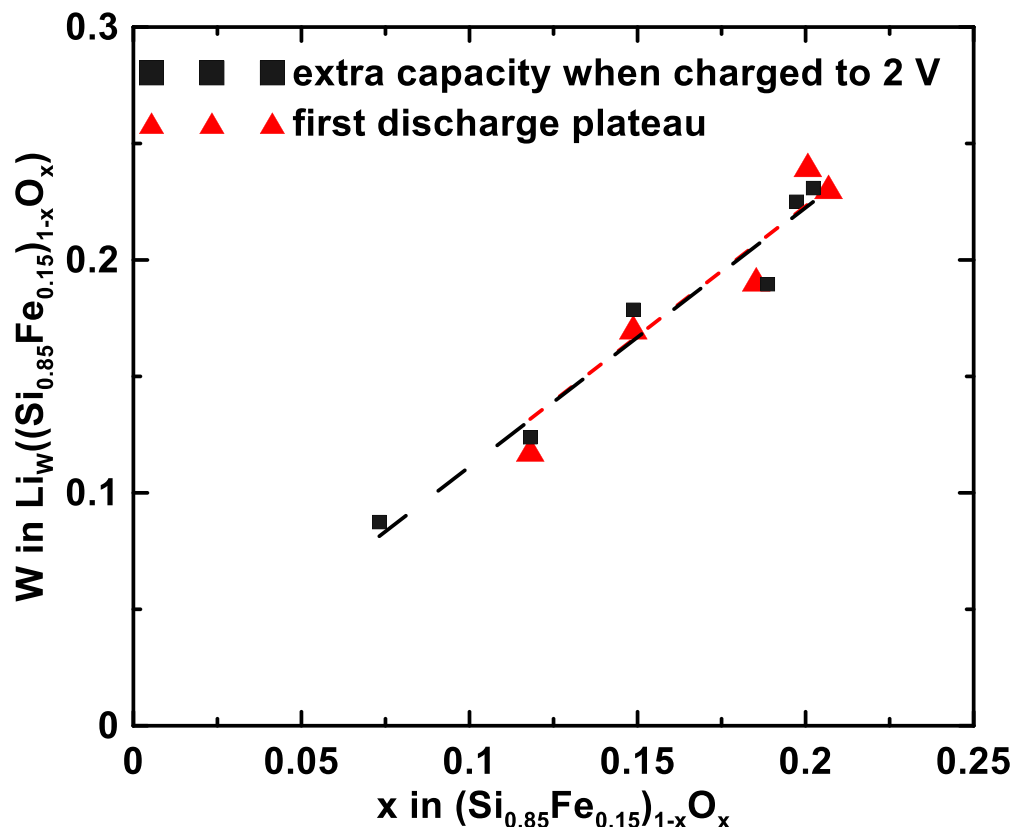


Figure 6. The amount of Li inserted per mole of (Si_{0.85}Fe_{0.15})_{1-x}O_x during the initial ~0.5 V oxygen-related potential plateau and the amount of Li extracted between 0.9 V and 2 V versus the oxygen content, x.

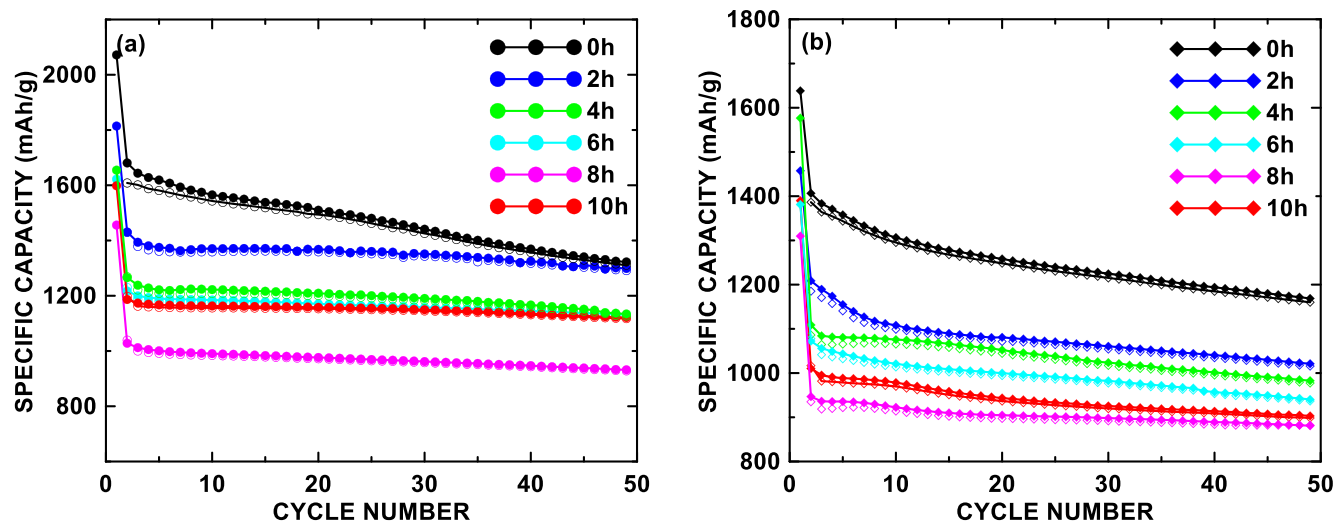


Figure 7. (a) Specific capacity versus cycle number of $\text{Si}_{85}\text{Fe}_{15}\text{O}_x$ alloys with different air milling times. (b) Specific capacity versus cycle number of $\text{Si}_{85}\text{Fe}_{15}\text{O}_x$ alloys with different air milling times after annealing to 800°C .

$\text{Si}_{85}\text{Fe}_{15}\text{O}_x$ alloys. The ICE decreases when the oxygen content increases from 7 to 20 at. %, because of the irreversible formation of Li_4SiO_4 during first lithiation. There are no significant differences in ICE between the last three compositions (6–10 h samples). This is consistent with their oxygen content: after 6 h, there is no significant change in the oxygen content even when the air milling time was increased to 10 h. Figure S8 shows the CE plots of ball milled $\text{Si}_{85}\text{Fe}_{15}\text{O}_x$ alloys made at different air milling times. The air milled samples generally have better CE performance (~ 99.6 – 99.8% , from cycles 60–100) than the non air-exposed $\text{Si}_{85}\text{Fe}_{15}$ alloy (~ 99.2 – 99.7% , from cycles 60–100), indicating less side reaction with electrolyte during cycling.

Figure 4 shows the potential profiles and differential capacity curves of $\text{Si}_{85}\text{Fe}_{15}\text{O}_x$ alloys as milled and after different thermal treatments. The potential profiles of the 600°C annealed alloys are very similar to the as-milled alloys, except that the initial lithiation high potential plateaus have become reduced in potential and in capacity. For the 800°C samples and for air milling times less than 6 h, the high potential plateaus have completely disappeared. This effect is associated with the “healing” of oxygen defects during thermal processing.³² The similarity between the as-milled alloys and the 600°C annealed alloys reflects the similarity also in the XRD patterns and TEM images of these samples. For the $\text{Si}_{85}\text{Fe}_{15}\text{O}_x$ (0 h) RT and 600°C alloys, the lithiation differential capacity curve comprises an initial sharp peak at about 0.29 V and 0.18 V, respectively, which likely correspond to a nucleation and growth process as the alloy is initially lithiated. However, this peak is not present for $\text{Si}_{85}\text{Fe}_{15}\text{O}_x$ (2–10 h) alloys. Presumably, the initial lithiation process at high voltage due to the high potential oxygen plateau precludes the nucleation and growth process in the oxygen-containing alloys. For the 800°C annealed samples milled less than 6 h in air where the high potential plateau is not present, a sharp peak corresponding to the nucleation and growth of lithiated phases during the first lithiation is present at about 0.14 V. Again, for longer milling times, when the high potential plateau precludes nucleation and growth, this sharp peak disappears.

For the 800°C annealed alloys, a flat plateau is observed in the potential curves during delithiation for the $\text{Si}_{85}\text{Fe}_{15}\text{O}_x$ alloys with short air milling time and a corresponding delithiation peak appears near 0.43 V in their differential capacity curves. This peak is associated with the delithiation of $\text{Li}_{15}\text{Si}_4$ and indicates that this phase has been formed during the previous lithiation half-cycle. The formation of $\text{Li}_{15}\text{Si}_4$ occurs if the active Si phase in the alloy has aggregated or is poorly connected to the inactive phase and is associated with capacity fade.^{13,18,35,37,38} The sharpest 0.43 V peak

appears for the 800°C annealed 0 h air milled alloy, where the crystallization of Si can be identified from the XRD pattern (Fig. 2b). Indeed, the presence of the 0.43 V peak in the differential capacity curves is directly correlated with the size of the crystalline Si peak shown in Fig. 2b. As demonstrated in Figs. 2b and 4, alloys with higher air milling time are more effective at suppressing Si crystallization during annealing and suppressing $\text{Li}_{15}\text{Si}_4$ formation. The $\text{Si}_{85}\text{Fe}_{15}\text{O}_x$ (6–10 h) alloys are particularly thermally stable, with both Si crystallization and $\text{Li}_{15}\text{Si}_4$ formation being nearly completely suppressed in these samples after heating to 800°C .

The cycling performance of the 800°C heated alloys are shown in Fig. 7b. After heating, the alloys have a lower capacity than the unheated alloys. This is likely due to the disproportionation of Si-O species to Si and inactive SiO_2 , resulting in the isolation of active Si regions, making them inaccessible towards lithiation, as has been previously observed in heated SiO_x .³⁴ Severe capacity fade occurs for the heated alloys with short air milling time. As the air milling time is increased (and Si crystallization and $\text{Li}_{15}\text{Si}_4$ formation is suppressed), capacity fade is reduced. In particular, the 800°C annealed $\text{Si}_{85}\text{Fe}_{15}\text{O}_x$ (10 h) alloy can maintain a high capacity of about 1000 mAh/g with almost no loss after 50 cycles. This corresponds to a volumetric capacity of 1140 Ah/L (see Supplemental Information). This good thermal stability enables these alloys to be amenable towards high-temperature processing.

To demonstrate the usefulness of such particles, the $\text{Si}_{85}\text{Fe}_{15}\text{O}_x$ (10 h) alloy was incorporated into graphite particles via mechanofusion, as described in Ref. 29. Figures S9a and S9b show SEM images of the $\text{Si}_{85}\text{Fe}_{15}\text{O}_x$ (10 h)/graphite composite powder and its electrode cross section, respectively. According to Fig. S9a, some alloy particles are found adhered on or embedded in the graphite particle surfaces. Many are loosely dispersed amongst the graphite particles. Many of the particles that did not embed in the graphite are larger than $1\ \mu\text{m}$ or part of agglomerates that are larger than $1\ \mu\text{m}$. Some of the agglomerated particles in the SEM image are as large as $5\ \mu\text{m}$. Figure S9b shows a cross section of the $\text{Si}_{85}\text{Fe}_{15}\text{O}_x$ (10 h)/graphite composite particles. Almost all the void space within the graphite particles has been filled with alloy particles as a result of the mechanofusion embedding process. It was observed that all the embedded particles exist as primary particles that are less than $1\ \mu\text{m}$ in size. Based on the larger size of the non-embedded particles, it is believed that further particle size reduction and breaking up the secondary particles into primary particles is needed to improve the embedded alloy fraction.

The partially embedded $\text{Si}_{85}\text{Fe}_{15}\text{O}_x$ (10 h)/graphite composite particles were carbon coated via CVD processing at 800°C to avoid

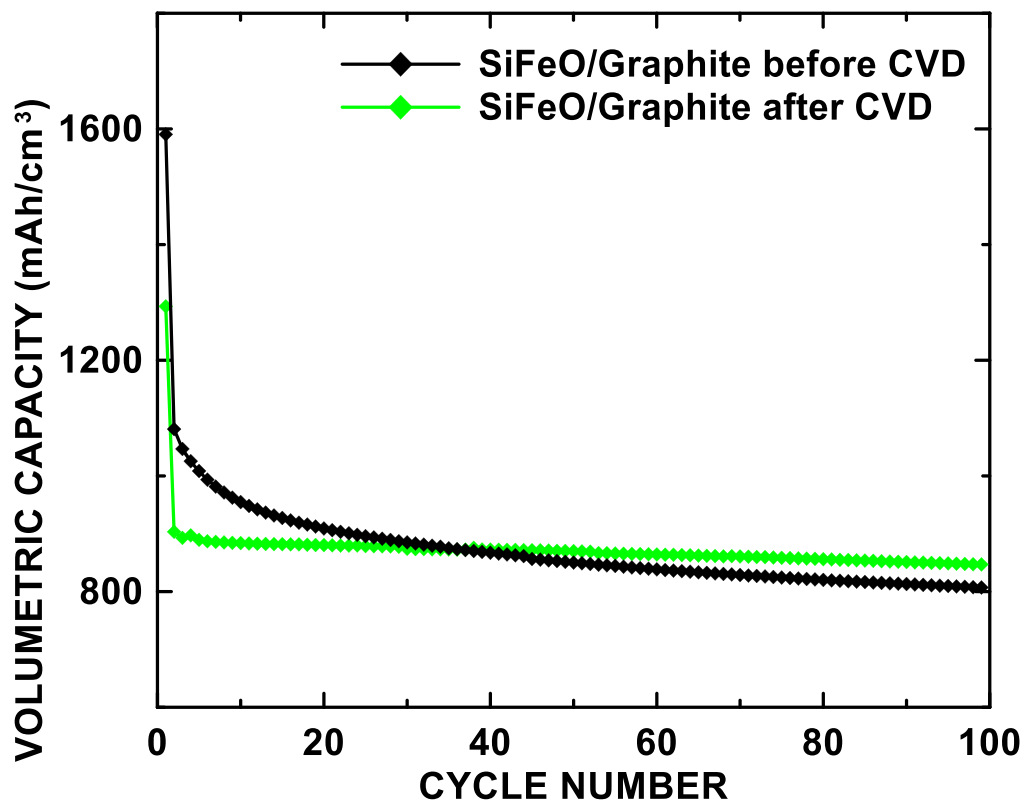


Figure 8. Volumetric capacity versus cycle number of $\text{Si}_{85}\text{Fe}_{15}\text{O}_x(10\text{ h})$ /graphite composite alloys before and after CVD carbon coating.

electrolyte infiltration. Figure 8 shows the capacity vs. cycle number of these alloy/graphite composite particles with and without CVD coating in PVDF binder and with no special electrolyte additives (i.e. no FEC). Under such conditions, Si-based alloys are known to have extremely poor cycling performance. However, remarkably good cycling can be obtained with the carbon coated composite particles even without the use of advanced binders or electrolyte additives. This good cycling was achieved even though the alloy in the $\text{Si}_{85}\text{Fe}_{15}\text{O}_x(10\text{ h})$ /graphite composite particles made here was only partially embedded. We believe that such particles are highly desirable by battery manufacturers as drop-in solutions to increase battery energy density without requiring any changes to binder or electrolyte formulation and that further improvements can be made by reducing the alloy particle size to improve the embedding process. Such investigations are currently underway in our lab utilizing thermally stable alloys, such as the $\text{Si}_{85}\text{Fe}_{15}\text{O}_x$ alloys developed here.

Conclusions

Reactive gas milling of an 85:15 ratio of Si and Fe powders for different times in air resulted in the formation of $\text{Si}_{85}\text{Fe}_{15}\text{O}_x$ alloys with $0.07 \leq x \leq 0.2$. Increasing air milling time resulted in reduced capacity, but significantly increased capacity retention and thermal stability towards Si crystallization. In particular, 10 h air milled $\text{Si}_{85}\text{Fe}_{15}\text{O}_x$ alloy had excellent thermal stability and good cycling characteristics. After heating to 800 °C, this alloy retained a high volumetric capacity of 1140 Ah/L after 50 cycles with little fade or $\text{Li}_{15}\text{Si}_4$ formation during cycling. The usefulness of this alloy was demonstrated by incorporating it into carbon-coated graphite composite particles that can cycle well even without the use of advanced binders or electrolyte additives.

Acknowledgments

The authors would like to thank the Natural Sciences and Engineering Research Council of Canada (NSERC) and NOVONIX Battery Technology Solutions, Inc. for funding.

ORCID

M. N. Obrovac  <https://orcid.org/0000-0001-5509-3185>

References

1. P. Zuo and G. Yin, *J. Alloys Compd.*, **414**, 265 (2006).
2. Y. Wang, J. M. Lee, and X. Wang, *Int. J. Hydrogen Energy*, **35**, 1669 (2010).
3. Y. Wang, S. Cao, M. Kalinina, L. Zheng, L. Li, M. Zhu, and M. N. Obrovac, *J. Electrochem. Soc.*, **164**, A3006 (2017).
4. X. Zhao, R. J. Sanderson, M. A. Al-Maghrabi, R. A. Dunlap, and M. N. Obrovac, *J. Electrochem. Soc.*, **164**, A1165 (2017).
5. Y. L. Kim, H. Y. Lee, S. W. Jang, S. H. Lim, S. J. Lee, H. K. Baik, Y. S. Yoon, and S. M. Lee, *Electrochim. Acta*, **48**, 2593 (2003).
6. Z. Du, S. N. Ellis, R. A. Dunlap, and M. N. Obrovac, *J. Electrochem. Soc.*, **163**, A13 (2016).
7. K. M. Lee, Y. S. Lee, Y. W. Kim, Y. K. Sun, and S. M. Lee, *J. Alloys Compd.*, **472**, 461 (2009).
8. H.-Y. Lee and S.-M. Lee, *J. Power Sources*, **112**, 649 (2002).
9. M. D. Fleischauer, J. M. Topple, and J. R. Dahn, *Electrochem. Solid-State Lett.*, **8**, A137 (2005).
10. Z. Du, H. Liu, S. N. Ellis, R. A. Dunlap, M. Zhu, and M. N. Obrovac, *J. Electrochem. Soc.*, **163**, A1275 (2016).
11. W. He, H. Tian, F. Xin, and W. Han, *J. Mater. Chem. A*, **3**, 17956 (2015).
12. X. Li, Y. Zheng, Z. Li, Y. Liu, H. Huang, Q. Wang, and C. Dong, *Mater. Chem. Phys.*, **243**, 122666 (2020).
13. M. Ruttner, V. Sizios, M. Winter, and T. Placke, *ACS Appl. Energy Mater.*, **3**, 743 (2020).
14. H. Wang, S. Fan, Y. Cao, H. Yang, X. Ai, and F. Zhong, *ACS Appl. Mater. Interfaces*, **12**, 30503 (2020).
15. Y. Chen, J. Qian, Y. Cao, H. Yang, and X. Ai, *ACS Appl. Mater. Interfaces*, **4**, 3753 (2012).
16. L. MacEachern, R. A. Dunlap, and M. N. Obrovac, *J. Electrochem. Soc.*, **162**, A2319 (2015).
17. Y. Cao, B. Scott, R. A. Dunlap, J. Wang, and M. N. Obrovac, *J. Electrochem. Soc.*, **165**, 1 (2018).
18. Z. Du, R. A. Dunlap, and M. N. Obrovac, *J. Electrochem. Soc.*, **163**, A2011 (2016).
19. M. Oh, I. Kim, H. J. Lee, S. Hyun, and C. Kang, *RSC Adv.*, **8**, 9168 (2018).
20. L. MacEachern, R. A. Dunlap, and M. N. Obrovac, *J. Electrochem. Soc.*, **162**, A229 (2015).
21. Y. Du, Z. Yang, L. Bai, F. Ding, H. Jin, Y. Yang, T. D. Lam, G. Hou, and F. Yuan, *Chem. Nano Mat.*, **7**, 467 (2021).
22. H.-T. Kwon, A.-R. Park, S.-S. Lee, H. Cho, H. Jung, and C.-M. Park, *J. Electrochem. Soc.*, **166**, A2221 (2019).

23. J. Jang, I. Kang, M. S. Kim, J. H. Kim, Y. S. Lee, K. W. Yi, and Y. W. Cho, *J. Mater. Sci.*, **52**, 5027 (2017).
24. M. Rutttert, V. Siozios, M. Winter, and T. Placke, *Zeitschrift Fur Anorg. Und Allg. Chemie*, **645**, 248 (2019).
25. L. J. Krause, T. Brandt, V. L. Chevrier, and L. D. Jensen, *J. Electrochem. Soc.*, **164**, A2277 (2017).
26. A. Hohl, T. Wieder, P. A. Van Aken, T. E. Weirich, G. Denninger, M. Vidal, S. Oswald, C. Deneke, J. Mayer, and H. Fuess, *J. Non. Cryst. Solids*, **320**, 255 (2003).
27. M. A. Al-Maghrabi, J. Suzuki, R. J. Sanderson, V. L. Chevrier, R. A. Dunlap, and J. R. Dahn, *J. Electrochem. Soc.*, **160**, 1587 (2013).
28. Y. Cao, J. C. Bennett, R. A. Dunlap, and M. N. Obrovac, *Chem. Mater.*, **30**, 7418 (2018).
29. Y. Cao, T. D. Hatchard, R. A. Dunlap, and M. N. Obrovac, *J. Mater. Chem. A*, **7**, 8335 (2019).
30. T. D. Hatchard, A. Genkin, and M. N. Obrovac, *AIP Adv.*, **7**, 045201 (2017).
31. S. Cao, J. C. Bennett, Y. Wang, S. Gracious, M. Zhu, and M. N. Obrovac, *J. Power Sources*, **438**, 227003 (2019).
32. Y. Cao, R. A. Dunlap, and M. N. Obrovac, *J. Electrochem. Soc.*, **167**, 110501 (2020).
33. E. Gaffet, N. Malhouroux, and M. Abdellaoui, *J. Alloys Compd.*, **194**, 339 (1993).
34. C. M. Park, W. Choi, Y. Hwa, J. H. Kim, G. Jeong, and H. J. Sohn, *J. Mater. Chem.*, **20**, 4854 (2010).
35. D. S. M. Iaboni and M. N. Obrovac, *J. Electrochem. Soc.*, **163**, A255 (2016).
36. M. N. Obrovac and L. J. Krause, *J. Electrochem. Soc.*, **154**, A103 (2007).
37. Z. Du, T. D. Hatchard, R. A. Dunlap, and M. N. Obrovac, *J. Electrochem. Soc.*, **162**, A1858 (2015).
38. H. Liu, M. Zhu, Z. Du, and M. N. Obrovac, *J. Electrochem. Soc.*, **163**, A192 (2016).
39. J. Y. Kim, A. Y. Kim, G. Liu, J. Y. Woo, H. Kim, and J. K. Lee, *ACS Appl. Mater. Interfaces*, **10**, 8692 (2018).
40. W. Wu, J. Shi, Y. Liang, F. Liu, Y. Peng, and H. Yang, *Phys. Chem. Chem. Phys.*, **17**, 13451 (2015).
41. T. Chen, J. Wu, Q. Zhang, and X. Su, *J. Power Sources*, **363**, 126 (2017).
42. T. Hirose, M. Morishita, H. Yoshitake, and T. Sakai, *Solid State Ionics*, **303**, 154 (2017).